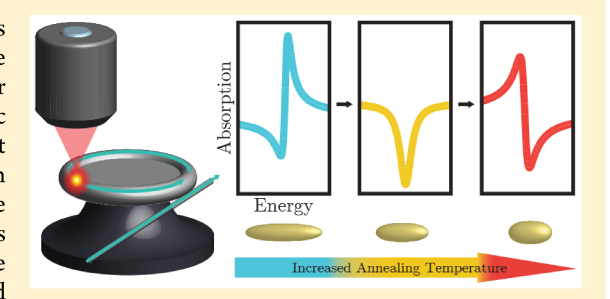
Sculpting Fano Resonances To Control Photonic-Plasmonic **Hybridization**

Niket Thakkar,[†] Morgan T. Rea,[‡] Kevin C. Smith,[§] Kevin D. Heylman,[‡] Steven C. Quillin,^{||} Kassandra A. Knapper,[‡] Erik H. Horak,[‡] David J. Masiello,^{*,†,||} and Randall H. Goldsmith^{*,‡}

Supporting Information

ABSTRACT: Hybrid photonic-plasmonic systems have tremendous potential as versatile platforms for the study and control of nanoscale light-matter interactions since their respective components have either high-quality factors or low mode volumes. Individual metallic nanoparticles deposited on optical microresonators provide an excellent example where ultrahigh-quality optical whispering-gallery modes can be combined with nanoscopic plasmonic mode volumes to maximize the system's photonic performance. Such optimization, however, is difficult in practice because of the inability to easily measure and tune critical system parameters. In this Letter, we present a general and practical method to determine the coupling strength and tailor the



degree of hybridization in composite optical microresonator-plasmonic nanoparticle systems based on experimentally measured absorption spectra. Specifically, we use thermal annealing to control the detuning between a metal nanoparticle's localized surface plasmon resonance and the whispering-gallery modes of an optical microresonator cavity. We demonstrate the ability to sculpt Fano resonance lineshapes in the absorption spectrum and infer system parameters critical to elucidating the underlying photonic-plasmonic hybridization. We show that including decoherence processes is necessary to capture the evolution of the lineshapes. As a result, thermal annealing allows us to directly tune the degree of hybridization and various hybrid mode quantities such as the quality factor and mode volume and ultimately maximize the Purcell factor to be 10⁴.

KEYWORDS: Microresonator, nanophotonics, Purcell effect, Fano interference

I ybrid photonic-plasmonic nanosystems, where optical modes of a dielectric cavity couple to collective charge oscillations of a metal nanoparticle, are gaining broad research interest as platforms for maximizing light-matter interactions, 1-7 enabling directional control of emission, 8,9 low-power nonlinear optics, 10 versatile optical interconnects, 11-15 and label-free single-molecule detection. 16-18 In particular, the Purcell factor, ¹⁹ a measure of an optical cavity mode's ability to enhance the spontaneous decay of a nearby emitter, has been shown to dramatically increase in hybrid systems over uncoupled photonic and plasmonic components.²⁰

In his original work, Purcell showed that this enhancement is proportional to the mode's quality factor, Q, which describes its temporal decay rate and therefore its ability to localize light in time, and inversely proportional to the mode's volume, V, which describes the volume occupied by the mode's field and therefore its ability to localize light in space. 19,21 Thus, hybrid photonic-plasmonic structures offer especially high Purcell enhancements due to their ability to combine a microphotonic cavity's unparalleled quality factor (over 108)22,23 with a plasmonic system's nanoscopic mode volume (down to 10^{-6} λ^3). 24,25

This divide-and-conquer strategy, where individual components with high Q and low V are coupled to maximize near-field enhancement, has found considerable success in a variety of implementations. 1,5,7,16,17,20,26-28 Still, in most cases, there is little control over the resulting enhancement factor and the frequency at which maximum enhancement occurs, limiting the use of these hybrid cavities in applications. Moreover, while Q and V are straightforward to determine in isolated, non-interacting systems, $^{23,29-31}$ their determination in the hybridized case requires an accurate estimation of the components' coupling strength, g_i and resulting degree of hybridization, θ_i both defined explicitly in the text below. Typically, this estimation is done via computationally expensive, multimaterial, multiscale, full-wave electrodynamics simulations. 20,26,32 A more versatile method to control and estimate components'

Received: August 3, 2017 Revised: September 27, 2017 Published: October 2, 2017

Department of Applied Mathematics, University of Washington, Seattle, Washington 98195-3925, United States

^{*}Department of Chemistry, University of Wisconsin-Madison, Madison, Wisconsin 53706-1322, United States

[§]Department of Physics, University of Washington, Seattle, Washington 98195-1560, United States

Department of Chemistry, University of Washington, Seattle, Washington 98195-1700, United States

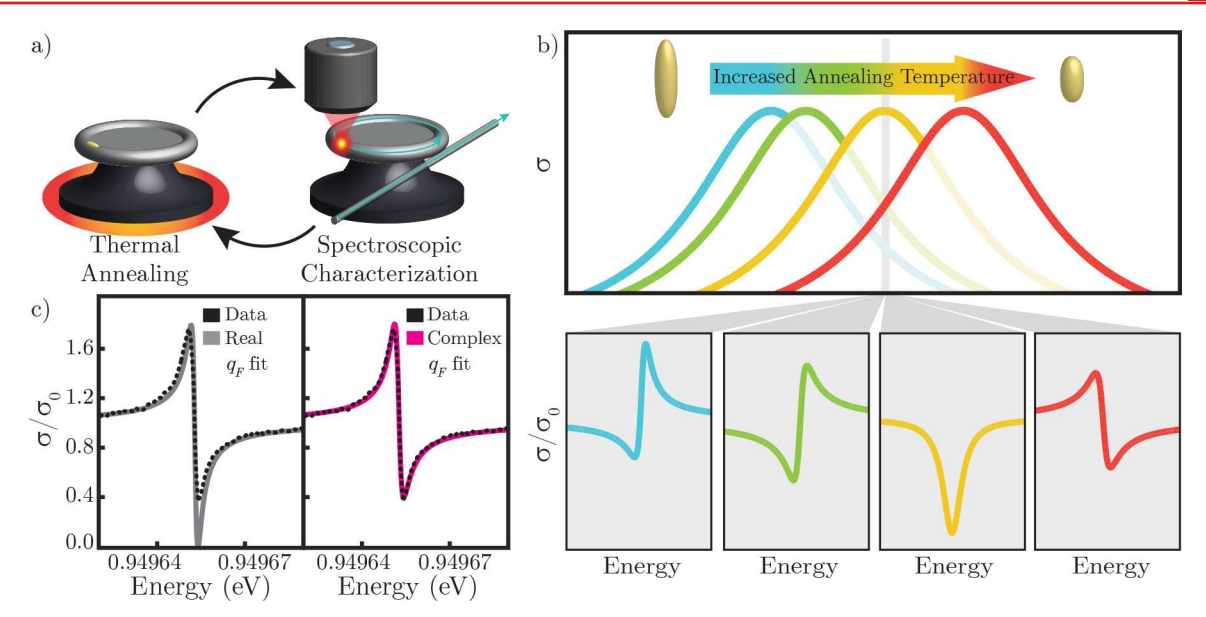


Figure 1. Fano resonances in a coupled toroidal WGM microresonator—plasmonic NR system. (a) Spectroscopic characterization of the coupled system is alternated with thermal annealing of the NR; at each annealing temperature, a separate absorption spectrum is recorded. (b) Increasing the thermal annealing temperature decreases the aspect ratio of the NR, increasing the plasmon resonance energy (top) and reshaping the Fano interference between a fixed WGM of the microresonator and the LSP (bottom). Note that NR aspect ratio changes are exaggerated to highlight the effects of thermal annealing. (c) Fits to experimental data (black) using the Fano line shape with a real q_F (gray dashed) cannot capture the incomplete destructive interference (vanishing absorption signal), while using the complex q_F in eq. 8 (pink dashed) results in an excellent fit.

coupling strength from experiment, as well as accounting for the largely unexplored role of decoherence in hybrid systems, is needed before photonic—plasmonic cavities can be used on a wider scale in nanophotonics applications.

In this Letter, using a plasmonic, metal nanorod (NR) and a toroidal whispering-gallery mode (WGM) microresonator²² (SI Section 1), where Fano resonances are diagnostic of photonicplasmonic hybridization, 33,34 we report a general method for the experimental determination of g and control of θ , as well as downstream quantities such as the hybridized Q and V, from the system's absorption spectrum. Our method entails the sculpting of Fano resonances by controlled thermal annealing of the metal nanorod. We demonstrate that proper inclusion of both photonic and plasmonic loss channels and the consequent role of decoherence in determining the Fano line shape is critical for accurate determination of the coupling strength. Finally, using an experiment-based approach, we show how the degree of hybridization can be optimized in practice to achieve Purcell enhancements on the order of 10⁴, in agreement with purely simulation-based studies of similar systems.²

The hybridized system's absorption spectrum contains the required information needed to determine its photonic properties, and here we demonstrate this by mixing the dipolar localized surface plasmon (LSP) of an individual gold nanorod with the optical modes of a silica toroidal WGM microresonator. Since the plasmonic nanorods examined are nonluminescent, a means of performing single-particle absorption spectroscopy on nonluminescent targets is required to investigate the hybridization. ^{33,35-39} As described previously, ³³ we use the microresonator as a single-particle, photothermal absorption spectrometer by monitoring via a coupled fiber the shift in a WGM that is detuned from the NR due to local heating from the laser excited NR. As the pump laser frequency is scanned, local heating by the NR varies in proportion to the particle's absorption cross section, resulting in observable shifts in the WGM transmission. Using a double-

modulation scheme, this method offers both high sensitivity, allowing us to resolve shifts in the WGM resonance of less than 100 Hz, and high spectral resolution, with fine spectra acquired at a resolution of \sim 5 μ eV.³³

As shown in Figure 1, characteristic Fano resonances appear in the NR absorption spectrum due to coherent interaction between the spectrally broad LSP and the spectrally narrow WGMs.³³ Each Fano resonance corresponds to a hybrid mode of the NR-microresonator cavity. Asymmetric lineshapes in the electron energy loss study of the autoionization of helium⁴⁰ were originally described by Fano and have since been found in a variety of optical^{34,41,42} and transport⁴³ experiments where interaction between a discrete state and a broad continuum results in characteristic, asymmetric spectral features. In the original work and since then, Fano resonances take the form

$$\frac{\sigma(\omega)}{\sigma_0(\omega)} = \left| \frac{q_F + \epsilon}{\epsilon + i} \right|^2 \tag{1}$$

where in our case $\sigma(\omega)/\sigma_0(\omega)$ is the absorption spectrum of the composite system normalized to that of the isolated NR, $\sigma_0(\omega)$, and $\varepsilon(\omega)$ is a dimensionless reduced frequency. $q_{\rm F}$ is the so-called Fano asymmetry parameter, which characterizes the degree of asymmetry in the resonance's line shape as a function of detuning between a discrete state and the continuum 33,34,40 and determines the spectral location ($\varepsilon(\omega)=-q_{\rm F}$) where destructive interference between the discrete state and the continuum results in a total loss of absorption.

Because the shape of the Fano resonance is tied to the LSP resonance frequency,³³ we can control the line shape by reducing the initially high aspect ratio (1:10) of the gold nanorod to shift the plasmon resonance. To that end, the entire resonator chip is annealed on a hot plate (Figure 1a) at 10 distinct temperatures ranging from 140–175 °C. Between annealing steps, the chip is allowed to cool to room temperature before measuring the corresponding absorption

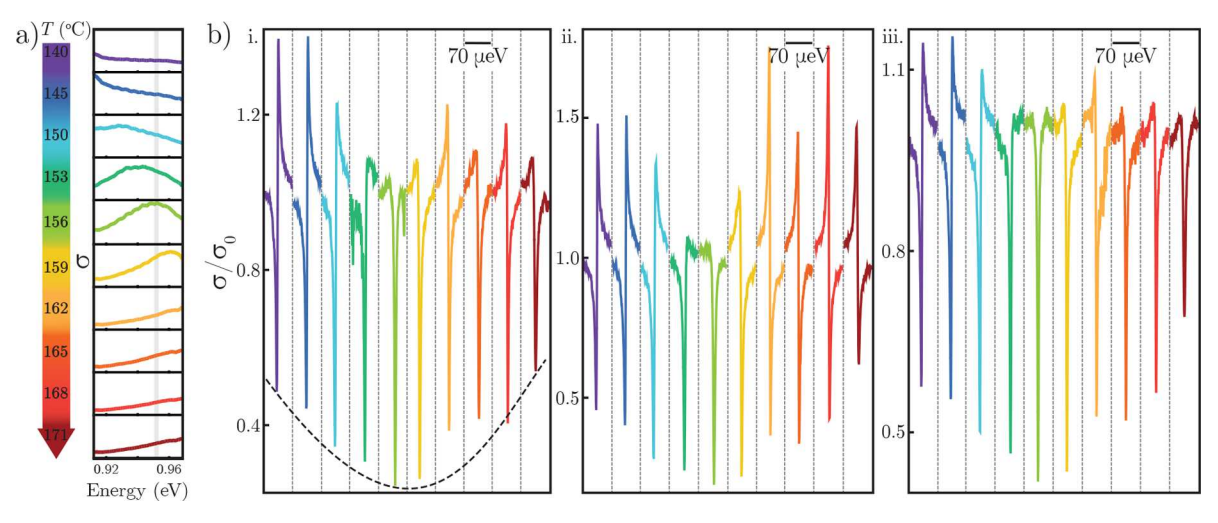


Figure 2. Sculpting Fano resonances by thermal annealing. (a) Low-resolution absorption spectra of a gold NR acquired at room temperature after annealing to the indicated temperature. (b) Evolution of three Fano resonances located within the gray region pictured in panel a, with colors in panel b representing the same temperatures as in panel a. Panels are centered at (i) 0.9496 eV, (ii) 0.9497 eV, and (iii) 0.9498 eV, and each panel is \sim 80 μ eV wide. Each panel within (i) tracks the same Fano resonance acquired at different annealing temperatures, thus each panel in (i) is of the same spectral region; the same is true for (ii) and (iii). The dashed line in (i) indicates the observed nonmonotonic envelope of Fano resonance depths.

spectrum. At these annealing temperatures, NR melting causes a self-limiting, monotonic, and irreversible blueshift in the LSP resonance, $^{44-46}$ while changes to the silica microresonator are negligible. Over the thermal range explored, the shifts in LSP resonance frequency suggest a softening in the aspect ratio from approximately (1:10) to (1:8). 47,48 This sculpting method was determined to be more controllable than other methods such as chemical etching 49,50 and laser heating. $^{51-53}$

Spectroscopic characterization can then be cycled with thermal annealing steps. In Figure 2a, low-resolution spectra (where Fano resonances are not visible) taken at room temperature after heating the chip to the indicated temperature display a systematic blue shift in the LSP absorption profile as expected; see Figure 1b top. Repeated high-resolution spectra of the same coupled WGM-LSP feature in a narrow spectral window (\sim 80 μ eV) show that Fano resonances due to WGM-LSP interaction changes shape as the LSP profile passes through the narrow window (Figure 2b) with the expected shift in asymmetry³³ (Figure 1b bottom, easily apparent). Surprisingly, no Fano resonances exhibit total destructive interference between the WGM and LSP, behavior repeated across multiple Fano resonances for multiple WGMs and across multiple NRs (SI Section 6). Thus, the line shape cannot be adequately fit by eq 1 because the equation predicts that the spectral line will always vanish at some point in the spectrum (Figure 1c, left). Indeed, when repeatedly displaying a normalized resonance in the same spectral window while the LSP energy is shifted via thermal annealing, an envelope is seen defining the depth of the Fano resonance where the depth appears to be a nonmonotonic function of the LSP energy. This experimental behavior challenges the canonical Fano interference mechanism and motivates the development of a more comprehensive theory.

Deformation of the Fano resonances as a function of LSP energy can be quantitatively understood by first considering the total electromagnetic field energy of the system, ⁵⁴

$$H = \sum_{mn} \int \frac{dV}{8\pi} \left[\frac{\partial}{\partial \omega} (\omega \varepsilon(\mathbf{x}, \, \omega))_{\omega_m} \mathbf{E}_m \cdot \mathbf{E}_n + \mathbf{B}_m \cdot \mathbf{B}_n \right]$$
(2)

where $\varepsilon(\mathbf{x},\omega)$ is the piecewise dielectric constant defined to be a free-electron gas in the NR,⁵⁵ 1.44 for silica in the resonator, and 1 elsewhere, and the total electric and magnetic fields are composed of contributions from the dipolar LSP mode (m,n=0) and the mutually orthogonal resonator modes (m,n=1,2,...). Restricting to a single WGM for simplicity and including a driving force on the LSP, the equations of motion associated with H are (SI Section 2)

$$\ddot{p}_{0} + \gamma_{0}\dot{p}_{0} + \omega_{0}^{2}p_{0} + g^{2}\omega_{0}^{2}p_{1} = \omega_{0}^{2}\sqrt{V_{0}}E_{\text{ext}}e^{-i\omega t}$$

$$\ddot{p}_{1} + \gamma_{1}\dot{p}_{1} + \omega_{1}^{2}p_{1} + g^{2}\omega_{1}^{2}p_{0} = 0$$
(3)

where only electric field mediated LSP-WGM interaction is considered. Here, p_0 is the generalized momentum describing the LSP's electric field (\mathbf{E}_0) , p_1 is the generalized momentum of the WGM (\mathbf{E}_1) , and the LSP is driven by a harmonically varying external source, $E_{\rm ext}$, modeling the frequency ω pump laser polarized along the NR long axis (Figure 1a). Both modes have associated frequencies, ω_0 or ω_1 , and mode volumes, V_0 or V_1 . Furthermore, via the cross terms in eq 2, they exchange energy through coupling characterized by g_1 , a dimensionless constant defined by

$$g^{2}p_{0}p_{1} = \int \frac{\mathrm{d}V}{8\pi} \left[\frac{\partial}{\partial\omega} (\omega \varepsilon(\omega, \mathbf{x}))_{\omega_{0}} \mathbf{E}_{0}(\mathbf{x}) \cdot \mathbf{E}_{1}(\mathbf{x}) + \frac{\partial}{\partial\omega} (\omega \varepsilon(\omega, \mathbf{x}))_{\omega_{1}} \mathbf{E}_{1}(\mathbf{x}) \cdot \mathbf{E}_{0}(\mathbf{x}) \right]$$
(4)

where $\mathbf{E}_0(\mathbf{x}) \cdot \mathbf{E}_1(\mathbf{x}) = \mathbf{E}_1(\mathbf{x}) \cdot \mathbf{E}_0(\mathbf{x})$ depends on the spatial overlap of the modes' fields and therefore on the NR's location and orientation on the microresonator surface (SI Section 2). As will be shown below, LSP and WGM losses are critical to describe the observed Fano interferences. Thus, we further model LSP and WGM losses with damping rates characterized by γ_0 and γ_1 added to the equations of motion.

It is instructive to first consider the frictionless limit (i.e., $\gamma_0 = \gamma_1 = 0$). In that case, eq 3 can be solved exactly through a coordinate rotation (SI Section 3), defining a set of

noninteracting normal modes, p_{\pm} , related to the original p_0 and p_1 by a rotation angle

$$\theta = \frac{1}{2} \tan^{-1} \left(\frac{2g^2 \omega_0 \omega_1}{\omega_0^2 - \omega_1^2} \right)$$
 (5)

which describes the degree of hybridization between the LSP and WGM modes. As expected, θ depends on both the LSP-WGM coupling g and detuning, $\omega_1 - \omega_0$. In the weak coupling limit $(g^2\omega_0\omega_1/(\omega_0^2-\omega_1^2)\ll 1)$, $\theta=0$ and no hybridization occurs, while in the strong coupling limit $(g^2\omega_0\omega_1/(\omega_0^2-\omega_1^2))$ \gg 1), $\theta = \pi/4$ and the normal modes are maximally mixed. θ , therefore, can be controlled via thermal annealing which will influence the detuning. In the more general case with losses (γ_0 $\neq 0, \gamma_1 \neq 0), \theta$ is not an exact degree of hybridization but can be used as a qualitative indicator of hybridization (SI Section 4). We find that our annealing process does not significantly modify the overlap of fields, which is proportional to g, but does alter the detuning between modes by shifting ω_0 (SI Section 7). Thus, thermal annealing allows us to optimize and understand the degree of hybridization for a given NR location and orientation on the resonator while keeping g constant.

The absorption cross section can be calculated with losses (friction) using standard methods to solve eq 3, giving the exact expression (SI Section 5)

$$\frac{\sigma(\omega)}{\sigma_0(\omega)} = \left| \frac{q_{\rm F} + \epsilon}{\epsilon + i} \right|^2 + \left| \frac{q_{\rm F} - i}{\epsilon + i} \right|^2 \frac{\text{Im } q_{\rm F}}{1 - \text{Im } q_{\rm F}}$$
(6)

where $\sigma_0(\omega)=(4\pi\omega\omega_0^2V_0/c){\rm Im}~Z_0^{-1}$ is the uncoupled LSP absorption cross section with $Z_0=\omega_0^2-\omega^2-i\omega\gamma_0$, and the second term characterizes a modification to the Fano profile (eq 1) which vanishes when the WGM is frictionless as ${\rm Im}~q_{\rm F}/(1-{\rm Im}~q_{\rm F})=\gamma_1/\Gamma$. The spectral location and width of the Fano resonance, here denoted by Ω and Γ , respectively, are defined by

$$\Omega^{2} = \omega_{1}^{2} - g_{1}^{4} \omega_{0}^{2} \omega_{1}^{2} \text{Re} Z_{0}^{-1}$$

$$\omega \Gamma = \omega \gamma_{1} + g_{1}^{4} \omega_{0}^{2} \omega_{1}^{2} \text{Im } Z_{0}^{-1}$$
(7)

both in general functions of ω but approximately constant in the weak coupling limit applicable here (SI Section 5). $\varepsilon(\omega) = (\omega^2 - \Omega^2)/\omega\Gamma$ is again a dimensionless reduced pump frequency in units of the Fano resonance line width away from resonance location and

$$q_{\rm F}(\omega) = \frac{\Omega^2 - \omega_1^2}{\omega \Gamma} + i \frac{\gamma_1}{\Gamma} \tag{8}$$

is the now complex-valued Fano asymmetry parameter.³⁴ Its real part characterizes shift in WGM frequency due to coupling with the LSP, and its imaginary part describes the fraction of the total Fano resonance line width attributed to WGM losses. In the limit where $\gamma_1 \rightarrow 0$ and the WGM has $Q \rightarrow \infty$, Im $q_F \rightarrow 0$ and the well-known purely real-valued Fano profile expression, eq 1, is recovered in eq 6. In that case, $q_F \approx 2(\omega_1 - \omega_0)/\gamma_0$, qualitatively explaining the observed shape change in Figure 2 as ω_0 , and the resulting degree of mixing, θ , are modified by thermal annealing. However, in this limit, the composite system absorption drops to zero when $\varepsilon(\omega) = -q_F$ implying $\omega = \omega_1$, on resonance with the WGM, in stark disagreement with experiment. In contrast, use of a complex-valued q_F , arising from the inclusion of loss in both WGM and LSP channels, enables excellent fitting of the Fano features

including the incomplete destructive interference as shown in Figure 1c. More generally, since the zero that appears in the original Fano expression is due to complete destructive interference between WGM and LSP, any process that degrades the phase relationship associated with the WGM and LSP oscillators would then manifest itself as a recovery of the vanishing spectral feature. Complex-valued $q_{\rm F}$ have also appeared in models of molecular and mesoscopic transport and in strongly coupled plasmonic systems. While this formalism has general applicability to other phenomena, this is the first time that it has been applied in hybrid photonic—plasmonic systems.

In analogy with the Redfield equation governing the spectroscopy of a two-level system coupled to an environment, decoherence can derive from population relaxation (T_1) , where energy is transferred from one level to another, or from pure dephasing (T_2^*) , where the phase degrades without transition between states due entirely to fluctuations of the environment.⁶² Our treatment connects the complex Fano resonance with relaxation in both the photonic and the plasmonic channels without the need to include pure dephasing. Much as population relaxation and pure dephasing can both contribute to homogeneous line widths, both processes can also be thought of as mechanisms of breaking time-reversal symmetry, which has previously been associated with complex Fano parameters.³⁴ Indeed, transport measurements have connected complex q_F to pure dephasing by demonstrating sharp reductions of pure dephasing at low temperatures leading to recoveries of destructive interference.4

In many past studies, 33,34 including Fano's original work, spectral resolution limitations also contributed to the Fano profile's shape and prevented a total loss of signal when $\epsilon(\omega)=-q_{\rm F}$. As a result, statistical analysis of spectra could be done with real-valued $q_{\rm F}$ but required additional scaling and offset parameters to accurately model measurements. Here, however, spectral resolution can not explain the systematic envelope in peak depths, Figure 2b (dotted black line). In fact, we see that the Fano profiles are better modeled by complex $q_{\rm F}$ shapes even as the spectral resolution is increased (SI Section 6), indicating that the finite WGM Q factor plays a crucial role in determining the Fano line shape. Thus, as we show in detail below, eq 6 is an important generalization of Fano's original work that is amenable to statistical analysis without scaling and offset parameters.

We can use our new theory to predict the evolution of the Fano profile throughout the thermal Fano sculpting process. The statistical fitting to the data is done in two steps (SI Section 7). First, low-resolution spectra, Figure 2a, are fit to $\sigma_0(\omega)$ to determine ω_0 at each annealing temperature. While these spectra are measured for the composite microresonator-NR system, the resolution is low enough such that only the broad Lorentzian envelope due to the plasmon resonance, and not the spectrally narrow Fano resonances, can be resolved. Next, we fit individual Fano resonances, experimentally measured via high resolution spectra, to eq 6 with ω_1 , γ_0 , γ_1 , and g as fit parameters, allowing us to use eq 8 to determine the measured dependence of q_F upon ω_0 .

A comparison of the measured (black dots) and predicted (solid curve) evolution of the Fano profile's shape is illustrated for a single Fano resonance in Figure 3. Here, fit results from a single Fano resonance at an intermediate temperature ($T_{\rm anneal}$ = 156 °C) are used to specify the LSP and WGM parameters and their coupling, g. Then, eq 8 is used to extrapolate and predict

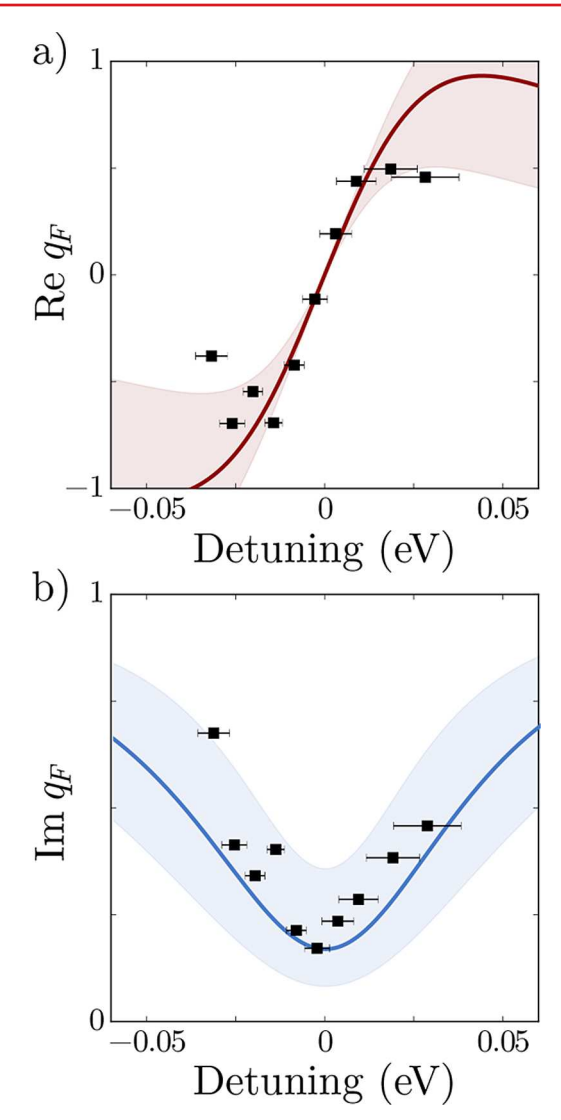


Figure 3. (a) Real and (b) imaginary parts of the Fano asymmetry parameter q_F as a function of the detuning, $\omega_1 - \omega_0$, for a single Fano resonance. Using ω_1 , γ_0 , γ_1 , and g as free parameters, experimentally measured Fano resonances are fit to eq 6, and q_F is computed using eq 8 (black squares). Theoretical predictions (red and blue lines) are generated using eq 6 in conjunction with the fit to the Fano line shape at a single intermediate temperature, here chosen to be 156 °C where the WGM and LSP modes are nearly degenerate ($\omega_1 \approx \omega_0$). Uncertainties in these predictions, which are here shown as one standard deviation intervals (shaded regions), are computed by randomly sampling ω_1 , γ_0 , γ_1 , and g from a normal distribution whose width is determined from uncertainties in the fit parameters. Horizontal error bars are determined from the uncertainty in ω_0 at each temperature (SI Section 7).

the Fano profile's shape for higher and lower LSP energy assuming the annealing process has no effect on the other parameters. Figure 3a and b shows that the measured evolution (black dots) for the real and imaginary parts of $q_{\rm F}$ agree well with the model's prediction (red and blue curves). This agreement tells us that the dominant effect of thermal annealing is to shift the LSP energy with little effect on the LSP-WGM field overlap, g. Comparisons to other Fano profile's evolutions yield a similar agreement (SI Section 7).

A broader comparison of the model and data is carried out by calculating the distribution of all experimentally observed complex q_F given parameters from the experiment. This test is

done for the real and imaginary parts of $q_{\rm F}$ in Figure 4, which shows the results from fits to 225 Fano resonances across three different NR-microresonator systems (red, blue, and green squares). Evolution is plotted as a function of detuning between ω_1 and ω_0 , and in both cases the data display a definitive trend. Theoretical distributions of $q_{\rm F}$ are calculated by taking $\hbar\gamma_0$ to be

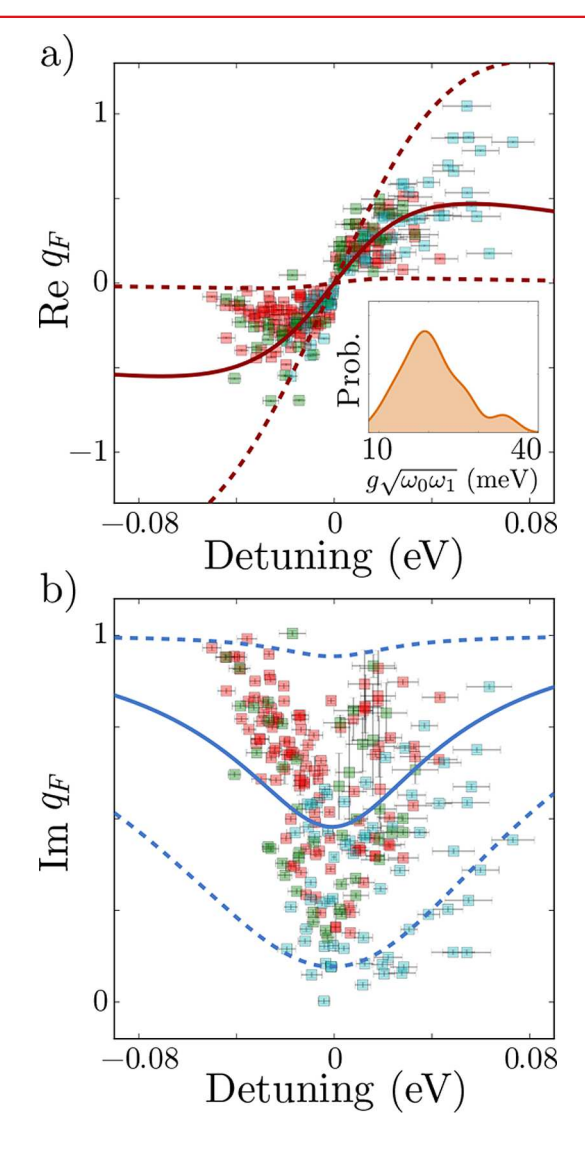


Figure 4. (a) Real and (b) imaginary parts of the Fano asymmetry parameter $q_{\rm F}$ as a function of WGM-LSP detuning, $\omega_1 - \omega_0$, for a collection of 225 Fano lineshapes. Results from statistical fitting to eq 6 are shown for three separate NR-microresonator systems (red, blue, and green squares). Blue squares correspond to a NR with a smaller relative unannealed LSP resonance frequency and thus represent data at higher detuning relative to red and green squares. Theoretical distributions of both the real and imaginary parts of $q_{\rm F}$ are determined from eq 8 using $\hbar \gamma_0 = 56.8$ meV, the average value from the data, along with randomly sampled WGM parameters and couplings. More specifically, ω_1 is sampled from a uniform distribution on the spectral range; γ_1 is sampled randomly from the fit results, and g is sampled from the estimated distribution of the couplings from the fit results (inset). This sampling process models the random location and orientation of the NR on the toroid surface and allows us to calculate 10⁴ randomly generated Fano resonances to determine the theoretical distribution of real and imaginary $q_{\rm F}$ as a function of detuning. We show both the average (solid line) as well as 95% confidence intervals (dashed lines) of the resulting distributions.

the average value from the data and calculating $q_{\rm F}$ for randomly sampled WGM parameters and coupling. Resulting distributions are plotted as an average value (solid line) and 95% confidence interval (dashed lines) in both panels a and b. We see that for both the real and imaginary parts the model captures the observed behavior under the assumption that all parameters but ω_0 are constant throughout the annealing process.

The excellent agreement between theory and observation in Figures 3 and 4 indicates that estimates of the LSP-WGM interaction energy based on our fit procedure are accurate, and indeed, our average coupling energy based on 225 Fano resonances is 22.0 meV, in the same range as other studies of hybridized photonic–plasmonic systems. ^{20,33,63} For a particular Fano resonance, statistical fitting to determine the coupling energy allows us to calculate a variety of important hybrid mode properties. Given the LSP energy and line width, the WGM energy and line width, and g, the parameters on the lefthand side of eqs 3 are fully specified. This system can then be rewritten as a set of coupled, first-order differential equations, and the corresponding coefficient matrix, A, can be diagonalized to specify the quasi-hybrid modes (QHMs) of the NR-microresonator system (SI Section 4). The QHMs, hybrid modes which incorporate losses and therefore have complex eigenvalues, 30,64,65 can then be used to calculate the hybrid mode fields, mode volumes, Purcell factors, and other properties.

We calculate the Purcell factor as an example of this procedure. LSP-WGM coupling produces two QHMs, one WGM dominated and the other LSP dominated. In both cases, the QHM electric field is a linear combination of LSP and WGM fields, $E_{QHM} = c_0E_0 + c_1E_1$, with c_0 and c_1 extracted from the eigenvectors of **A**. The QHM mode volume ⁶⁴ is then

$$V_{\text{QHM}} = \frac{\int dV \frac{\partial}{\partial \omega} (\omega \varepsilon(\omega, \mathbf{x}))_{\omega_{\text{QHM}}} |\mathbf{E}_{\text{QHM}}(\mathbf{x})|^2}{\max \left\{ \frac{\partial}{\partial \omega} (\omega \varepsilon(\omega, \mathbf{x}))_{\omega_{\text{QHM}}} |\mathbf{E}_{\text{QHM}}(\mathbf{x})|^2 \right\}}$$
(9)

where $\omega_{\rm QHM}$ is determined from the eigenvalue associated with the set of c_0 and c_1 for each hybridized mode. Expansion of $|E_{\rm QHM}|^2$ results in three terms proportional to V_0 , V_1 , and the overlap of $E_0 = -p_0 f_0$ and $E_1 = -p_1 f_1$, where f_0 and f_1 are the mode functions of the nanorod and toroid as dictated by the Helmholtz equation (SI Section 2). Both V_0 and V_1 can be determined through experiment 29,32 or simple, single-material, single-scale electrodynamics simulations, circumventing the need for computationally intensive multiscale methods. Meanwhile, the overlap term can be rewritten in terms of the statistically inferred coupling, g_0 , as expressed in eq 4. Finally, the Purcell factor, F_0 , can be calculated using $V_{\rm OHM}$:

$$F = \frac{3}{4\pi^2} \left(\frac{\lambda_{\text{QHM}}}{n} \right)^3 \text{Re} \left\{ \frac{Q_{\text{QHM}}}{V_{\text{QHM}}} \right\}$$
(10)

where $\lambda_{\rm QHM}$ is the wavelength associated with $\omega_{\rm QHM}$, n=1 is the refractive index at the location of the emitter proximal to the hybridized cavity (assumed to lie in the junction between the WGM resonator and the NR), and $Q_{\rm QHM}=\omega_{\rm QHM}/2\gamma_{\rm QHM}$ is the QHM quality factor, also determined from the eigenvalue associated with c_0 and c_1 (SI Section 8).

We can use this method to estimate the Purcell factor as a function of LSP energy throughout the Fano sculpting process. This process is shown in Figure 5 for the Fano resonance in

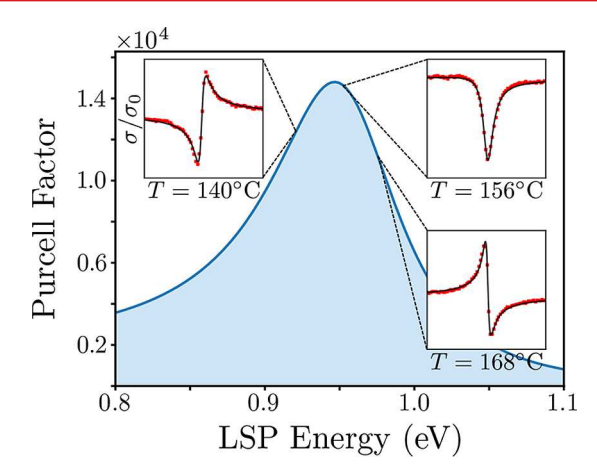


Figure 5. Purcell factor for one photonic—plasmonic QHM is displayed as a function of a microresonator WGM coupled to the LSP of an individual gold NR. Statistical fitting to the Fano resonance in Figure 3 at low annealing temperatures is used to determine the coupling of the nanorod to the WGM and predict the mode volume, quality factor, and Purcell factor of the hybridized system. The mode volume, determined by eq 9, is minimized when the LSP energy is degenerate with the WGM at $\omega_0 = \omega_1 = 0.9544$ eV. This minimum in the mode volume corresponds to a maximum value exceeding 10^4 for the Purcell factor of the QHM. The insets show the change in the Fano line shape as the LSP energy moves from below the WGM ($\omega_0 < \omega_1$), to degenerate with the WGM ($\omega_0 = \omega_1$), to above the WGM ($\omega_0 > \omega_1$).

Figure 3. We see that the Purcell factor is maximized when ω_0 = ω_1 , where the Fano line shape is symmetric (inset), while asymmetry in the Fano resonance indicates LSP-WGM hybridization is suboptimal. Due to the high density of WGM resonances supported by the resonator, the frequency at which this maximum occurs can be altered through selection of a different Fano resonance, thus allowing control over the spectral location of the maximum Purcell enhancement. Our maximum Purcell factor for the resonance shown is $\sim 10^4$ with $V_{\rm QHM} \sim 10^9$ nm³ and $Q_{\rm QHM} \sim 10^4$, in agreement with other estimates based on full-wave, multiscale simulation of this system²0 and estimates of similar systems. Notably, our estimate of the coupling is inferred from an experimental spectrum.

Using thermal annealing we have experimentally demonstrated how to sculpt the Fano resonances and control the degree of hybridization in a photonic-plasmonic system composed of a coupled WGM microresonator cavity and a plasmonic NR. Guided by analytical modeling, we find that decoherence from losses from both the WGM and LSP degrees of freedom are needed to capture the line shape of the Fano resonance, generalizing the Fano asymmetry parameter to be complex-valued. Further statistical treatment enables the prediction of the Fano line shape as a function of the experimentally controlled detuning between LSP and WGM resonances, in excellent agreement with experimental data. Taken together, our combined experimental, analytic, and statistical approach allows for extraction of critical optical parameters from experimental data, yielding new insights into the fundamental properties of hybridized photonic-plasmonic systems and enabling maximization of the light-matter

Methods. Sample Preparation. Toroidal microresonators of a 46 μ m major diameter and 5 μ m minor diameter,

consisting of a silica toroid on a silicon pillar, are lithographically fabricated using methods previously described. 33 To deposit the gold NRs, a $10\times$ diluted solution of gold NRs (25 nm diameter, 245 nm length, Nanopartz A12-25-1400) in water is dropcast for 30 s on the toroid chip.

Spectroscopy. Following our previously described apparatus,³³ light from a tunable probe laser (Newport TLB-6728) is evanescently coupled into the microresonator via a tapered optical fiber. The Pound-Drever-Hall (PDH) locking technique is used to lock to a high-Q WGM resonance. Meanwhile, a second laser, called the pump laser (Thorlabs TLK-L1300), is delivered top-down through an objective (Nikon 60×, 0.95 NA) and excites the NRs on the resonator's surface. Excitation of the NR is amplitude modulated at 2.01 kHz and leads to heat dissipation from the NR into the toroid, which causes a resonance shift of the WGM mode. A lock-in amplifier (Signal Recovery 7265) is then used to discern the 2.01 kHz component of the PDH error signal. This detected resonance shift can then be related to the amount of heat dissipated using numerical simulations (COMSOL) and the NR's photoluminescence quantum yield (assumed to be zero).

Thermal Annealing. The plasmon resonance is tuned via "thermal annealing" by placing the toroid chip on a hot plate at a given temperature for 5 min. The toroid chip is spectroscopically characterized after each annealing process once the toroid chip has cooled room temperature.

ASSOCIATED CONTENT

S Supporting Information

The Supporting Information is available free of charge on the ACS Publications website at DOI: 10.1021/acs.nanolett.7b03332.

Information on (i) experimental details, (ii) modeling the LSP-WGM interaction, (iii) frictionless case and derivation of the mixing angle, (iv) diagonalization of the equations of motion in the presence of friction, (v) the absorption cross-section in the presence of friction, (vi) the complex asymmetry parameter, (vii) statistical methods, and (viii) calculation of the Purcell factor (PDF)

AUTHOR INFORMATION

Corresponding Authors

*E-mail: masiello@chem.washington.edu.

*E-mail: rhg@chem.wisc.edu.

ORCID @

David J. Masiello: 0000-0002-1187-0920 Randall H. Goldsmith: 0000-0001-9083-8592

Author Contributions

N.T., M.T.R., K.C.S., and K.D.H. contributed equally to this work.

Notes

The authors declare no competing financial interest.

ACKNOWLEDGMENTS

This work was supported by the NSF under award numbers DMR-1610345 (R.H.G.), CHE-1664684 (D.J.M.), DGE-1256082 (N.T.), and DGE-1256259 (K.A.K.).

REFERENCES

- (1) Barth, M.; Schietinger, S.; Fischer, S.; Becker, J.; Nusse, N.; Aichele, T.; Löchel, B.; Sönnichsen, C.; Benson, O. *Nano Lett.* **2010**, 10, 891–895.
- (2) Yang, X.; Ishikawa, A.; Yin, X.; Zhang, X. ACS Nano 2011, 5, 2831–2838.
- (3) Luo, Y.; Chamanzar, M.; Apuzzo, A.; Salas-Montiel, R.; Nguyen, K. N.; Blaize, S.; Adibi, A. *Nano Lett.* **2015**, *15*, 849–856.
- (4) Cui, S.; Zhang, X.; Liu, T.-l.; Lee, J.; Bracher, D.; Ohno, K.; Awschalom, D.; Hu, E. L. ACS Photonics 2015, 2, 465–469.
- (5) Xiao, Y.-F.; Liu, Y.-C.; Li, B.-B.; Chen, Y.-L.; Li, Y.; Gong, Q. Phys. Rev. A: At, Mol., Opt. Phys. 2012, 85, 031805.
- (6) Benson, O. Nature 2011, 480, 193-199.
- (7) Ameling, R.; Giessen, H. Laser Photonics Rev. 2013, 7, 141-169.
- (8) López-García, M.; Galisteo-López, J. F.; Blanco, A.; Sánchez-Marcos, J.; López, C.; García-Martín, A. Small 2010, 6, 1757–1761.
- (9) Ding, B.; Hrelescu, C.; Arnold, N.; Isic, G.; Klar, T. A. *Nano Lett.* **2013**, *13*, 378–386.
- (10) Stolyarov, A. M.; Wei, L.; Shapira, O.; Sorin, F.; Chua, S. L.; Joannopoulos, J. D.; Fink, Y. *Nat. Photonics* **2012**, *6*, 229–233.
- (11) Guo, X.; Qiu, M.; Bao, J.; Wiley, B. J.; Yang, Q.; Zhang, X.; Ma, Y.; Yu, H.; Tong, L. Nano Lett. 2009, 9, 4515–4519.
- (12) Maksymov, I. S. Phys. Lett. A 2011, 375, 918-921.
- (13) Sun, S.; Badawy, A.-H. A.; Narayana, V.; El-Ghazawi, T.; Sorger, V. J. IEEE Photonics J. 2015, 7, 1–14.
- (14) Chamanzar, M.; Adibi, A. Opt. Express 2011, 19, 22292-22304.
- (15) Wang, X.; Morea, R.; Gonzalo, J.; Palpant, B. Nano Lett. 2015, 15, 2633–2639.
- (16) Dantham, V. R.; Holler, S.; Barbre, C.; Keng, D.; Kolchenko, V.; Arnold, S. *Nano Lett.* **2013**, *13*, 3347–3351.
- (17) Baaske, M. D.; Foreman, M. R.; Vollmer, F. Nat. Nanotechnol. **2014**, 9, 933–939.
- (18) De Angelis, F.; Patrini, M.; Das, G.; Maksymov, I.; Galli, M.; Businaro, L.; Andreani, L. C.; Di Fabrizio, E. *Nano Lett.* **2008**, *8*, 2321–2327.
- (19) Purcell, E. M. Phys. Rev. 1946, 69, 681.
- (20) Doeleman, H. M.; Verhagen, E.; Koenderink, A. F. ACS Photonics 2016, 3, 1943–1951.
- (21) Agio, M.; Cano, D. M. Nat. Photonics 2013, 7, 674-675.
- (22) Armani, D. K.; Kippenberg, T. J.; Spillane, S. M.; Vahala, K. J. *Nature* **2003**, 421, 925–928.
- (23) Vahala, K. J. Nature 2003, 424, 839-846.
- (24) Chikkaraddy, R.; de Nijs, B.; Benz, F.; Barrow, S. J.; Scherman, O. A.; Rosta, E.; Demetriadou, A.; Fox, P.; Hess, O.; Baumberg, J. J. *Nature* **2016**, *535*, 127–130.
- (25) Schuller, J. A.; Barnard, E. S.; Cai, W.; Jun, Y. C.; White, J. S.; Brongersma, M. L. *Nat. Mater.* **2010**, *9*, 193–204.
- (26) Min, B.; Ostby, E.; Sorger, V.; Ulin-Avila, E.; Yang, L.; Zhang, X.: Vahala, K. *Nature* **2009**. *457*. 455–458.
- (27) Foreman, M. R.; Vollmer, F. Phys. Rev. A: At., Mol., Opt. Phys. 2013, 88, 023831.
- (28) Foreman, M. R.; Vollmer, F. New J. Phys. 2013, 15, 083006.
- (29) Zhang, S.; Park, Y.-S.; Liu, Y.; Zentgraf, T.; Zhang, X. Opt. Express 2010, 18, 6048-6055.
- (30) Kristensen, P. T.; Hughes, S. ACS Photonics 2014, 1, 2-10.
- (31) Maier, S. A. Opt. Quantum Electron. 2006, 38, 257–267.
- (32) Kippenberg, T.; Spillane, S.; Vahala, K. Appl. Phys. Lett. 2004, 85, 6113-6115.
- (33) Heylman, K. D.; Thakkar, N.; Horak, E. H.; Quillin, S. C.; Cherqui, C.; Knapper, K. A.; Masiello, D. J.; Goldsmith, R. H. *Nat. Photonics* **2016**, *10*, 788–795.
- (34) Miroshnichenko, A. E.; Flach, S.; Kivshar, Y. S. Rev. Mod. Phys. 2010, 82, 2257.
- (35) Blancon, J.-C.; Paillet, M.; Tran, H. N.; Than, X. T.; Guebrou, S. A.; Ayari, A.; San Miguel, A.; Phan, N.-M.; Zahab, A.-A.; Sauvajo, J.-L.; et al. *Nat. Commun.* **2013**, *4*, 2542.
- (36) Yorulmaz, M.; Nizzero, S.; Hoggard, A.; Wang, L.-Y.; Cai, Y.-Y.; Su, M.-N.; Chang, W.-S.; Link, S. *Nano Lett.* **2015**, *15*, 3041–3047.

(37) Mader, M.; Reichel, J.; Hänsch, T. W.; Hunger, D. Nat. Commun. 2015, 6, 7249.

- (38) Kukura, P.; Celebrano, M.; Renn, A.; Sandoghdar, V. *Nano Lett.* **2009**, *9*, 926–929.
- (39) Berciaud, S.; Cognet, L.; Poulin, P.; Weisman, R. B.; Lounis, B. *Nano Lett.* **2007**, *7*, 1203–1207.
- (40) Fano, U. Phys. Rev. 1961, 124, 1866.
- (41) Liu, Y.-C.; Li, B.-B.; Xiao, Y.-F. Nanophotonics **2017**, 6, 789–811.
- (42) Lee, J.; Perdue, S. M.; Rodriguez Perez, A.; Apkarian, V. A. ACS Nano 2014, 8, 54–63.
- (43) Bärnthaler, A.; Rotter, S.; Libisch, F.; Burgdörfer, J.; Gehler, S.; Kuhl, U.; Stöckmann, H.-J. *Phys. Rev. Lett.* **2010**, *105*, 056801.
- (44) Liu, Y.; Mills, E. N.; Composto, R. J. J. Mater. Chem. 2009, 19, 2704–2709.
- (45) Kennedy, W. J.; Slinker, K. A.; Volk, B. L.; Koerner, H.; Godar, T. J.; Ehlert, G. J.; Baur, J. W. ACS Appl. Mater. Interfaces 2015, 7, 27624–27631.
- (46) Petrova, H.; Juste, J. P.; Pastoriza-Santos, I.; Hartland, G. V.; Liz-Marzán, L. M.; Mulvaney, P. Phys. Chem. Chem. Phys. 2006, 8, 814–821.
- (47) Link, S.; Mohamed, M. B.; El-Sayed, M. A. J. Phys. Chem. B 1999, 103, 3073-3077.
- (48) Hartland, G. V. J. Chem. Phys. 2002, 116, 8048-8055.
- (49) Tsung, C.-K.; Kou, X.; Shi, Q.; Zhang, J.; Yeung, M. H.; Wang, J.; Stucky, G. D. J. Am. Chem. Soc. 2006, 128, 5352-5353.
- (50) Zou, R.; Guo, X.; Yang, J.; Li, D.; Peng, F.; Zhang, L.; Wang, H.; Yu, H. CrystEngComm **2009**, 11, 2797–2803.
- (51) Link, S.; Burda, C.; Nikoobakht, B.; El-Sayed, M. A. J. Phys. Chem. B 2000, 104, 6152-6163.
- (52) Desantis, C. J.; Huang, D.; Zhang, H.; Hogan, N. J.; Zhao, H.; Zhang, Y.; Manjavacas, A.; Zhang, Y.; Chang, W.-S.; Norlander, P.; et al. *J. Phys. Chem. C* **2016**, *120*, 20518–20524.
- (53) Taylor, A. B.; Siddiquee, A. M.; Chon, J. W. ACS Nano 2014, 8, 12071–12079.
- (54) Schwinger, J.; DeRaad, L. L., Jr.; Milton, K. A.; Tsai, W.-Y. Classical Electrodynamics; Westview Press, 1998.
- (55) Ashcroft, N. W.; Mermin, N. D. Solid State Physics; Cengage Learning, 2011.
- (56) Kobayashi, K.; Aikawa, H.; Katsumoto, S.; Iye, Y. *Phys. Rev. Lett.* **2002**, *88*, 256806.
- (57) Clerk, A.; Waintal, X.; Brouwer, P. Phys. Rev. Lett. 2001, 86, 4636.
- (58) Sheikholeslami, S. N.; García-Etxarri, A.; Dionne, J. A. *Nano Lett.* **2011**, *11*, 3927–3934.
- (59) Yang, J.; Perrin, M.; Lalanne, P. Phys. Rev. X 2015, 5, 021008.
- (60) Zhang, W.; Govorov, A. O. Phys. Rev. B: Condens. Matter Mater. Phys. 2011, 84, 081405.
- (61) He, Y.; Zhu, K.-D. J. Opt. Soc. Am. B 2013, 30, 868-873.
- (62) Nitzan, A. Chemical Dynamics in Condensed Phases: Relaxation, Transfer and Reactions in Condensed Molecular Systems; Oxford University Press, 2006.
- (63) Langbein, D. J. Phys. Chem. Solids 1971, 32, 1657-1667.
- (64) Sauvan, C.; Hugonin, J. P.; Maksymov, I. S.; Lalanne, P. Phys. Rev. Lett. 2013, 110, 237401.
- (65) Leung, P. T.; Liu, S. Y.; Young, K. Phys. Rev. A: At, Mol., Opt. Phys. 1994, 49, 3057–3067.